

## INTERACTION OF THE MAGNETOROTATIONAL INSTABILITY WITH HYDRODYNAMIC TURBULENCE IN ACCRETION DISKS

JARED C. WORKMAN<sup>1,2</sup> AND PHILIP J. ARMITAGE<sup>1,2</sup>

*ApJ, in press*

### ABSTRACT

Accretion disks in which angular momentum transport is dominated by the magnetorotational instability (MRI) can also possess additional, purely hydrodynamic, drivers of turbulence. Even when the hydrodynamic processes, on their own, generate negligible levels of transport, they may still affect the evolution of the disk via their influence on the MRI. Here, we study the interaction between the MRI and hydrodynamic turbulence using local MRI simulations that include hydrodynamic forcing. As expected, we find that hydrodynamic forcing is generally negligible if it yields a saturated kinetic energy density that is small compared to the value generated by the MRI. For stronger hydrodynamic forcing levels, we find that hydrodynamic turbulence modifies transport, with the effect varying depending upon the spatial scale of hydrodynamic driving. Large scale forcing boosts transport by an amount that is approximately linear in the forcing strength, and leaves the character of the MRI (for example the ratio between Maxwell and Reynolds stresses) unchanged, up to the point at which the forced turbulence is an order of magnitude stronger than that generated by the MRI. Low amplitude small scale forcing may modestly suppress the MRI. We conclude that the impact of hydrodynamic turbulence on the MRI is generically ignorable in cases, such as convection, where the additional turbulence arises due to the accretion energy liberated by the MRI itself. Hydrodynamic turbulence may affect (and either enhance or suppress) the MRI if it is both strong, and driven by independent mechanisms such as self-gravity, supernovae, or solid-gas interactions in multiphase protoplanetary disks.

*Subject headings:* accretion, accretion disks — hydrodynamics — instabilities — MHD — turbulence

### 1. INTRODUCTION

The magnetorotational (MRI) or Balbus-Hawley instability (Velikov 1959; Chandrasekhar 1961; Balbus & Hawley 1991, 1998) underpins the most important — and possibly only — source of outward angular momentum transport in a wide class of well-ionized accretion disks. The MRI destabilizes disk flows in which  $d\Omega^2/dr < 0$ , and leads to a state of sustained magnetohydrodynamic (MHD) turbulence that transports angular momentum outward (Hawley, Gammie & Balbus 1995; Brandenburg et al. 1995; Armitage 1998; Hawley 2000; Papaloizou & Nelson 2003; Hirose, Krolik & Stone 2006). The majority of the transport is mediated by Maxwell rather than Reynolds stresses. Following convention, the efficiency of angular momentum transport within disks is measured via an equivalent Shakura-Sunyaev (1973)  $\alpha$  parameter, which can be expressed in terms of the fluctuating velocity and magnetic fields as,

$$\alpha P_0 = \rho v_r \delta v_\phi + \frac{B_r B_\phi}{\mu_0}, \quad (1)$$

where  $P_0$  is the thermal pressure. The first term on the right-hand side of this equation represents the Reynolds (or fluid) stress and the second term represents the Maxwell (or magnetic) stress. There is no strict equivalence between the evolution of MHD turbulent disks and models that assume an  $\alpha$  shear viscosity

(Balbus & Hawley 1998; Pessah, Chan & Psaltis 2008), but for our purposes  $\alpha$  is a convenient measure of the efficiency of angular momentum transport.

The fact that the MRI dominates the transport of angular momentum within accretion flows does not, of course, imply that other sources of turbulence do not exist within disks. The most striking example occurs in galactic disks, in which turbulence can be driven by thermal instabilities and supernova explosions in regions that are unstable to the MRI (Piontek & Ostriker 2005). However, even in “normal” accretion disks around stars or compact objects there are numerous possibilities, including self-gravity in sufficiently massive disks (Toomre 1964), convection (Stone & Balbus 1996), and Kelvin-Helmholtz instabilities excited by the interaction between gaseous and solid components of protoplanetary disks (Cuzzi, Dobrovolskis & Champney 1993). Additional fluid motions can also be driven within disks due to the gravitational influence of embedded planets (Bate et al. 2002) or binary companions (Spruit et al. 1987), though the wave-like fluid motions induced by these sources are different from those initiated by turbulence. Some of these processes may drive fluid motions within the disk whose kinetic energy density is comparable to that resulting from the MRI. In particular, a self-gravitating disk can remain stable against fragmentation while generating an effective  $\alpha \simeq 10^{-1}$  (Gammie 2001; Rice, Lodato & Armitage 2005) — as large or larger than that produced by the MRI. Since the fluid motions resulting from hydrodynamic processes are uncorrelated with the MRI, it is reasonable to suspect that there could be non-trivial interactions between the MRI and other turbulent processes in disks within which both are operating

<sup>1</sup> JILA, Campus Box 440, University of Colorado, Boulder CO 80309; workmanj@colorado.edu, pja@jilau1.colorado.edu

<sup>2</sup> Department of Astrophysical and Planetary Sciences, University of Colorado, Boulder CO 80309

simultaneously. Indeed, Fromag et al. (2004) found that in a self-gravitating, MRI-turbulent disk, the strength of the angular momentum transport from the self-gravity was both weaker, and had a different time-dependence, when compared to a disk in which self-gravity alone was at work. This result is striking, since the disk simulated by Fromag et al. (2004) was dominated by low-order (azimuthal wavenumber  $m = 2$ ) self-gravitating structure whose scale was much larger than the most unstable MRI scales.

In detail, different drivers of hydrodynamic turbulence may influence the MRI in a unique manner, requiring a case-by-case study (self-gravity, for example, is a special case since it *does* yield outward transport of angular momentum, whereas most other hydrodynamic mechanisms yield negligible or even inward transport). We do not address such subtleties here, but rather study how generic driven hydrodynamic turbulence of specified strength interacts with the MRI. One's expectation is obviously that hydrodynamic turbulence that is weak (say, in terms of the saturated value of the kinetic energy density) compared to that driven by the MRI ought to leave the MRI unscathed, with significant interaction developing when the two sources of turbulence are of comparable strength. Very strong turbulence can amplify magnetic fields in the disk *independent* of the MRI, though this may not necessarily be accompanied by angular momentum transport. Our goal in this paper is to test such order of magnitude intuition.

The focus of this paper is on small-scales, which can be captured most effectively using local shearing-box simulations. Such simulations have significant limitations that must be borne in mind. In particular, the strength of angular momentum transport in zero-net flux simulations with purely numerical viscosity and magnetic diffusivity has a marked dependence on numerical resolution (Gardiner & Stone 2005; Fromang & Papaloizou 2007). Moreover, when physical values for the transport coefficients *are* used (as in this paper) the strength of turbulence depends upon the magnetic Prandtl number  $Pm \equiv \nu/\eta$  as well as on the Reynolds number (Lesur & Longaretti 2007; Fromang et al. 2007). What this means for real disks — which when highly ionized have values of the diffusivity  $\eta$  and viscosity  $\nu$  that are much smaller than can currently be simulated — is unclear, but an obvious implication for numerical experiments is that the absolute value of  $\alpha$  derived from shearing-box simulations must be viewed with caution. For the time being, constraints derived from modeling of observed systems may be more reliable (King, Pringle & Livio 2007). For this reason, our focus here is on how the strength of angular momentum transport varies in the presence of additional hydrodynamic turbulence, rather than its absolute value.

The plan of this paper is as follows. In §2 we describe the set-up for our runs, which make use of the PENCIL MHD code previously employed for both disk and turbulence calculations (e.g. Haugen, Brandenburg & Dobler 2004). In §3 we present results, which concentrate on the influence of different levels of hydrodynamic turbulence on the saturation level, structure, and angular momentum transport efficiency of the MRI. These results are summarized and discussed in §4.

## 2. METHODS

We use the PENCIL Code<sup>1</sup> to solve the dynamical equations used to describe a local, magnetized patch of an accretion disk in the co-rotating frame. The PENCIL Code solves the equations of compressible MHD in non-conservation form using sixth order spatial derivatives and third order temporal derivatives. The PENCIL Code has been used previously to study the MRI (Brandenburg et al. 1995), and has been shown to yield similar results to calculations performed using ZEUS and similar algorithms (Hawley, Gammie & Balbus 1995; Balbus & Hawley 1998). One important difference between PENCIL and ZEUS is that PENCIL requires the use of explicit diffusive terms to maintain stability. PENCIL is a fixed grid, Eulerian code, that is parallelized using MPI.

### 2.1. Equations

We follow the motion of a magnetized parcel of isothermal gas in the co-rotating frame. A local, Cartesian co-ordinate system is used, in which  $x$  represents the radial direction,  $y$  the azimuthal direction, and  $z$  the vertical direction. The equations of motion describing the system are derived by solving for deviations in the flow velocity  $\mathbf{u}$  from the Keplerian shear flow  $U_y(x) = (-3/2)\Omega x$ , where  $\Omega$  is the local background rotation rate (Brandenburg et al. 1995; Wisdom & Tremaine 1988).

Using the framework described above, the momentum equation is given by

$$\begin{aligned} \frac{\partial \mathbf{u}}{\partial t} = & -u_y^{(0)} \frac{\partial \mathbf{u}}{\partial y} - (\mathbf{u} \cdot \nabla \mathbf{u}) + 2\Omega u_y - \frac{1}{2}\Omega u_x \\ & - \frac{\nabla P}{\rho} + \frac{\mathbf{J} \times \mathbf{B}}{\rho} + \vec{F} + \nu_h \nabla^6 \mathbf{u} \end{aligned} \quad (2)$$

where  $\mathbf{u}$  is the velocity vector,  $P$  is the pressure,  $\rho$  is the density,  $\mathbf{J}$  is the current,  $\mathbf{B}$  is the magnetic field, and  $u_y^{(0)}$  is the background Keplerian shear. The terms in equation (2) correspond to: advection due to the background flow, advection of the perturbed velocity field, Coriolis and shear effects, pressure gradients, the Lorentz force, our forcing term (to be described in the next section) and viscous terms. We neglect the effects of vertical gravity both for the sake of computational economy, and because it is likely irrelevant for this study focusing on the interplay between the MRI and forced hydrodynamic turbulence. The viscous term  $\nu_h \nabla^6 \mathbf{u}$  describes so-called hyperviscous dissipation, specified by a parameter  $\nu_h$ . We use hyperviscosity to limit the effects of dissipation to the smallest scales and thereby extend our inertial range. For reviews of the effects of hyperviscosity on MHD simulations and a derivation of the hyperviscous term see Brandenburg & Sarson (2002) and Johansen & Klahr (2005).

The continuity equation is,

$$\frac{\partial \rho}{\partial t} = -u_y^{(0)} \frac{\partial \rho}{\partial y} - \nabla \cdot (\rho \mathbf{u}) \quad (3)$$

where the first term comes from advection due to the background flow and the second term refers to the stan-

<sup>1</sup> The PENCIL Code and its documentation are available at <http://www.nordita.org/software/pencil-code/>

ward mass flux. We use upwinding rather than diffusive terms to stabilize the mass conservation equation.

The final equation describes the evolution of the magnetic vector potential. PENCIL solves for the vector potential  $\mathbf{A}$  rather than the magnetic field  $\mathbf{B} = \nabla \times \mathbf{A}$ , which ensures a solenoidal (divergence free) magnetic field. The equation for the evolution of the vector potential is given by

$$\frac{\partial \mathbf{A}}{\partial t} = -u_y^{(0)} \frac{\partial \mathbf{A}}{\partial y} + \frac{3}{2} A_y \hat{\mathbf{x}} + \mathbf{u} \times (\nabla \times \mathbf{A}) + \eta_h \nabla^6 \mathbf{A}, \quad (4)$$

where the first term describes advection of the potential due to the background flow, the second term describes magnetic stretching due to shear, the third term describes the standard electromotive force, and the last term is the hyperdiffusive resistivity.

The final equation needed to close the system is the energy equation. We use an isothermal equation of state so this is simply  $P = \rho c_s^2$ , where  $c_s$  is the sound speed.

### 2.2. Forcing Term

Our goal in applying hydrodynamic forcing is to mimic the effects of hydrodynamic turbulence that is generated within the disk by mechanisms that are independent of the MRI. There are many possible approaches to accomplishing this, that vary depending upon whether the forcing is applied throughout the volume or only at the boundaries, and in the temporal and spatial scales involved. The ‘‘best’’ approach evidently depends upon the physics one seeks to mimic – forcing that is gravitationally driven, for example, would logically be written as the gradient of a potential function. For most of our runs we use a forcing term that injects energy throughout the volume at large scales (physically, this would be roughly the disk scale height). In the hydrodynamic regime this energy then cascades down to smaller scales where it is eventually dissipated (by viscosity at very small physical scales in a real disk, by hyperviscous dissipation at the grid scale in the simulations. We have also considered the effect of forcing the fluid on small spatial scales. In either case we adopt the forcing function introduced in Haugen et. al. (2004) which is given by

$$F(\mathbf{x}, t) = \mathbf{f}_{\mathbf{k}} N e^{[i\mathbf{k}(t) \cdot \mathbf{x} + i\phi(t)]}. \quad (5)$$

In this function the wavevector  $\mathbf{k}(t)$  and  $\phi(t) \in [-\pi, \pi]$  are chosen randomly at every time step guaranteeing that the forcing due to the function is uncorrelated in time. In order to ensure that the energy injection rate is independent of the time step is it normalized (using dimensional arguments) by setting,

$$N = f_0 c_s^{3/2} \sqrt{|\mathbf{k}|/\delta t}, \quad (6)$$

where the scalar  $f_0$  defines the amplitude of the resulting forcing. We discuss how we set  $f_0$  in the next Section. At each time step a random wavevector  $\mathbf{k}$  is selected from a certain range in  $k$  space along with a unit vector  $\mathbf{e}$ . These vectors are then used in the construction of the argument of the exponent as well as in the creation of

$$\mathbf{f}_{\mathbf{k}} = \frac{\mathbf{k} \times \mathbf{e}}{\sqrt{k^2 - (\mathbf{k} \cdot \mathbf{e})^2}} \quad (7)$$

which describes a nonhelical, transverse wave.

### 2.3. Setup

We choose a box sized  $(2\pi)^3$  with a resolution of  $160^3$ . The boundary conditions in the y and z directions are periodic and those in the x direction are shearing. Shearing sheet boundary conditions are described in Hawley, Gammie & Balbus (1995). We initialize the system with a density of  $\rho = 1$ , a sound speed  $c_s = 1$ , and an angular rotation rate of  $\Omega = 0.2$ . This scaling returns a box size of  $2\pi H/5$ . We include hyperviscosity to stabilize the scheme at the grid scale. The coefficients for the fluid viscosity and the magnetic resistivity are set equal to each other yielding a (hyperviscous / hyperresistive) Prandtl number ( $\nu_h/\eta_h$ ) of 1 for most simulations. Our hyperviscous and hyperresistive Reynolds numbers for grid scale shocks are 75. One technical point to be borne in mind when comparing our results with other MRI simulations is that we use a cubical domain rather than one elongated in the azimuthal direction. A cubical domain maximizes the range between the dissipation scale and the forcing scale, which necessarily has power on the *smallest* dimension of the domain. The uniform resolution in the three spatial directions ensures that hyperviscous and hyperresistive dissipation act isotropically. We do not see any significant differences between our results and prior simulations that we could ascribe to the differing simulation domains.

For our first simulation we initiate the MRI by setting up a magnetic field in the z direction that has the form  $A_0 \cos(kx)\hat{\mathbf{z}}$  where  $A_0 = 0.05$ . This yields a plasma  $\beta$  (defined as the ratio of the gas pressure to the magnetic pressure) of  $\beta = 800$  at the peak of the magnetic field. The instability is seeded by perturbing the velocity field with random gaussian fluctuations whose magnitude is of the order of  $10^{-3}c_s$ . With this setup the most unstable wavelength for the MRI, given by  $\lambda_c = 2\pi V_{a_z}/\sqrt{3}\Omega$  (Balbus & Hawley 1991), is resolved across 23 grid points. We do not use any forcing for the initial run which is intended to allow the MRI to develop into a saturated state. After evolving the simulation to 20 orbits we stop it at this point and create a restart dump. From here we restart the MRI only simulation and let it run for  $\sim 130$  more orbits. We call this simulation  $0f_0$  and it is our ‘fiducial’ run with which we compare all subsequent runs.

### 2.4. Large Scale Forcing

Once the MRI simulation is completed we begin several sets of hydrodynamic simulations with equivalent parameters but no magnetic fields. To these simulations we add the forcing function given by equation (5). We force the simulations around  $k = 1.5$  to simulate the effects of generic hydrodynamic turbulence being input at scales slightly smaller than our simulation domain. We force slightly interior to the boundaries to avoid issues with the boundary conditions. The forcing injects energy into the box at large scales, which then cascades down in the normal hydrodynamic manner. We run hydrodynamic simulations with varying values for  $f_0$  until the time averaged level of kinetic energy in the hydrodynamic simulations, due to the forcing function, approximately matches the time averaged level of kinetic energy in our MRI only run  $0f_0$ . We label our hydrodynamic only run as HL and allow it to run for  $\sim 150$  orbits.

Having determined the appropriate value for  $f_0$  we initialize six runs starting from the fully saturated MRI state we saved at 20 orbits in the MRI only case. We implement forcing from this point onward in each of the simulations with values of  $[\frac{1}{2}f_0, 1f_0, 2f_0, 4f_0, 8f_0, 16f_0]$  and run the simulations for approximately 130 orbits each. We label each run by the value of  $f_0$ ; HL is the purely hydrodynamical (large scale) run,  $0f_0$  is the fiducial MRI only run,  $.5f_0$  corresponds to the run with half strength forcing, and so on. The details of each run are summarized in Table 1.

In addition to the simulations described above we also ran four others with some of the underlying physics modified. The goal of these runs was to test how robust our results are to plausible changes in the forcing function (which is essentially arbitrary) and plasma microphysics. In two simulations we changed the time scale over which the forcing function switches to new wave vectors. The function is still defined and normalized as described by Equation (5) except that new vectors are now selected at intervals of  $P = 2\pi/\Omega$ . This is the natural resonance timescale for the disk. We run two simulations with this altered forcing, both starting at the fiducial 20 orbital periods and running out until 150 periods, one having  $2f_0$  and the other  $8f_0$  as their forcing amplitudes. We label these runs  $2f_0l$  and  $8f_0l$ , where the  $l$  indicates the long term nature of the forcing function.

Our final two large scale forcing simulations are motivated by the work of Lesur & Longaretti (2007) and Fromang et al. (2007) who demonstrate a link between the value of the magnetic Prandtl number  $\nu/\eta$  and the saturation level of magnetic turbulence. We initialize two forced runs at 20 orbits with a  $2f_0$  forcing amplitude (as this seems to correspond to the demarcation between the standard MRI behavior and that influenced by the hydrodynamic forcing) and run them to 150 orbits. For one run, labeled  $2f_0p4$  we increase the hyperviscous coefficient by a factor of four to correspond to a four fold increase in the Prandtl number. For the other run, labeled  $2f_0p.25$  we reduce the value of the hyperresistive coefficient to correspond to a four fold decrease in the Prandtl number.

### 2.5. Small Scale Forcing

In addition to examining the effects of large scale forcing we explore a (smaller) range of simulations where we input energy at a much smaller scale. Once again we set up a non forced MRI simulations with conditions equivalent to those described above. We run this to 20 orbits and save the values at this point. We then allow the unforced MRI to run to  $\sim 110$  orbits and label this run  $0sf_0$  where the  $s$  indicates the small scale forcing.

We then repeat the process, described above, of determining the value of the forcing strength parameter  $sf_0$  which produces a saturated kinetic energy level in a purely hydrodynamical run which is approximately equal to that produced in the fiducial MRI run, except now forcing at  $k = 40$ . This value is chosen as it represents small scales within our inertial range which are not yet affected by dissipation due to numerical effects. Having obtained an approximate match between the kinetic energy densities in the MRI-only and hydrodynamic runs, we label the forcing amplitude as  $sf_0$  and implement a series of forced runs starting from the fiducial 20 orbit

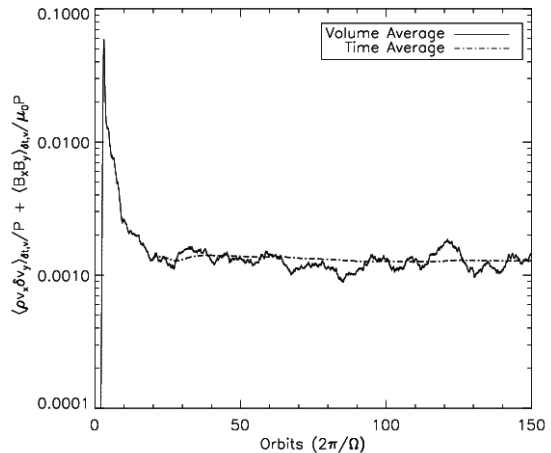


FIG. 1.— Time and volume averages (equations 9 and 8) of the transport coefficient,  $\alpha$  (equation 1) for the fiducial MRI run ( $0f_0$ ).

point using multiples of this value. These runs are labeled  $1sf_0$ ,  $2sf_0$ , and  $4sf_0$ .

## 3. RESULTS

Due to the fluctuating nature of turbulent quantities both spatial and temporal averaging is needed in order to obtain reproducible values for quantities such as the saturated magnetic field strength (Winters, Balbus & Hawley 2003; Papaloizou & Nelson 2003). We present results in terms of the volume average as a function of time, given by

$$\langle F(t) \rangle = \frac{1}{V} \int F(t) dV, \quad (8)$$

and in terms of a running time average given by

$$\langle F \rangle_{\delta t} = \frac{1}{t - t_0} \int_{t_0}^t \langle F(t) \rangle dt. \quad (9)$$

We use the latter quantity to assess whether our runs are long enough to attain convergence. We note that our run length has been chosen to be just sufficient to yield clear discrimination between the different forcing cases — much longer runs would be required to measure quantities to percent level precision.

### 3.1. Large Scale Forcing Runs

#### 3.1.1. Fiducial Run ( $0f_0$ )

We compare all of our runs to a fiducial non-forced MRI configuration. This run displays the characteristic behavior of MRI simulations (Brandenburg et al. 1995; Balbus & Hawley 1998). There is an initial exponential growth phase which amplifies all components of the magnetic and velocity fields, which reach peak amplitude at  $\sim 3$  orbits. After the peak there is a gradual reduction in all quantities until they saturate at a (fluctuating) level several orders of magnitude above their initial levels (except for  $B_z^2$  which, in these zero-net flux simulations, saturates at a level below its initial value). The saturated state is sustained and all quantities remain approximately constant until we stop the run at orbit  $\sim 150$ .

Figure 1 shows the total transport coefficient  $\alpha$  for the MRI only case. The behavior is as described above: an

Model	MHD	$f_0$	$\beta^{(a)}$	Grid	Size	$\lambda_c/\delta_z^{(b)}$	Orbits	$\langle \alpha \rangle_{\delta t, \mathbf{v}}^{(c)}$	$\nu/\eta$
HL	No	0	800	$160^3$	$(2\pi)^3$	23.1	150	-1e-7	NA
$0f_0$	Yes	0	800	$160^3$	$(2\pi)^3$	23.1	150	.00132	1
$.5f_0$	Yes	$\frac{1}{2}$	800	$160^3$	$(2\pi)^3$	23.1	150	.00127	1
$1f_0$	Yes	1	800	$160^3$	$(2\pi)^3$	23.1	150	.00163	1
$2f_0$	Yes	2	800	$160^3$	$(2\pi)^3$	23.1	150	.00187	1
$4f_0$	Yes	4	800	$160^3$	$(2\pi)^3$	23.1	150	.00319	1
$8f_0$	Yes	8	800	$160^3$	$(2\pi)^3$	23.1	150	.00510	1
$16f_0$	Yes	16	800	$160^3$	$(2\pi)^3$	23.1	150	.00764	1
$2f_0l$	Yes	2	800	$160^3$	$(2\pi)^3$	23.1	150	.0021	1
$8f_0l$	Yes	8	800	$160^3$	$(2\pi)^3$	23.1	150	.0048	1
$2f_0p4$	Yes	2	800	$160^3$	$(2\pi)^3$	23.1	150	.0031	4
$2f_0p.25$	Yes	2	800	$160^3$	$(2\pi)^3$	23.1	150	.0023	.25
HS	No	0	800	$160^3$	$(2\pi)^3$	23.1	150	4.2e-5	NA
$0sf_0$	Yes	0	800	$160^3$	$(2\pi)^3$	23.1	109	.0016	1
$1sf_0$	Yes	1	800	$160^3$	$(2\pi)^3$	23.1	124	.0008	1
$2sf_0$	Yes	2	800	$160^3$	$(2\pi)^3$	23.1	115	.00078	1
$4sf_0$	Yes	4	800	$160^3$	$(2\pi)^3$	23.1	115	.0026	1

TABLE 1

MODEL PARAMETERS. NOTES: <sup>(a)</sup>THE MAXIMAL VALUE OF  $\beta = P_{gas}/P_{magnetic}$ , AT  $t = 0$ ; <sup>(b)</sup> $\lambda_c = 2\pi V_{Az}/\sqrt{3}\Omega$ ; <sup>(c)</sup>DENOTES A TIME AND VOLUME AVERAGE FROM THE 20TH ORBIT UNTIL THE SIMULATION'S CONCLUSION

exponential increase in  $\alpha$  followed by a decay to reach a saturated state. The saturated value of  $\alpha$  is around  $1.3 \times 10^{-3}$ . As has been found in all prior simulations, the level of transport associated with the magnetic stresses is almost an order of magnitude higher than that associated with the fluid stresses.

The MRI-only run serves two purposes. First, we use it as a reference for comparison with the forced runs. For this comparison, we compute running averages from the MRI-only run starting at orbit 20, thereby excluding the initial (unphysical) exponential growth and decay phase. Second, we use the snapshot generated at orbit 20 as an initial condition for the forced runs. These forced runs thereby model the effect of additional turbulence on an already saturated disk. We do not study how strong forcing would impact the linear growth phase of the MRI, as it seems unlikely that this is relevant to any physical system.

### 3.1.2. Hydro Run (HL)

We next ran several forced, non-MHD simulations, in order to find the value of the forcing amplitude (defined through  $f_0$ ) that yields hydrodynamic turbulence of the same strength as that obtained in the MRI-only run. MHD and non-MHD turbulence can be physically different (Sridhar & Goldreich 1994), so there is no unique definition of equivalent strength. We define an equivalent hydrodynamic run as one which yields close to the same value of the saturated kinetic energy density as the MRI-only run<sup>3</sup>. Numerically, we found that a value of  $f_0 = 0.0035$  yielded reasonable agreement (at a level of about 10% between orbits 80 and 150). For this matched case Figure 2 shows how the running time averages of the kinetic energy compare in the MRI-only and hydro-only runs. Convergence of the kinetic energy in the box is rather slow in the hydrodynamic case (possibly due to the low level of viscosity, since lower resolution test runs converged more rapidly), but the level of the agreement at the end of the runs is sufficient for our purposes.

Figure 3 shows the running time average of the fluid  $\alpha$  in the hydrodynamic only reference run with this value

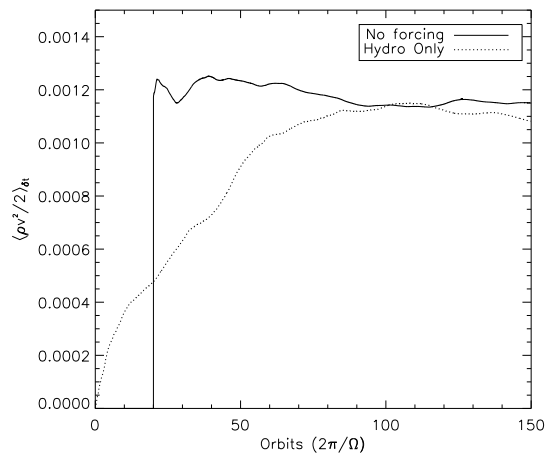


FIG. 2.— Running time averages (equation 9) of the kinetic energy for the unforced MRI run ( $0f_0$ ) and the hydrodynamic run (HL). In the hydrodynamic run forcing was used. The time averages for the MRI run are begun at 20 orbits to prevent contamination from the initial exponential phase of the instability. The mean value of the time averages agree to within  $\sim 10\%$  after orbit 80.

of  $f_0$ . As expected for randomly forced hydrodynamic turbulence, the level of transport obtained is consistent with zero and certainly negligible compared with either the Maxwell or Reynolds stresses generated in the MRI-case. This result is important as we are explicitly looking at the effects of large scale hydrodynamic turbulence on the MRI. If a particular forcing function were to generate a non-zero value for  $\alpha$  it would be difficult to separate its effects on transport from that of the MRI.

### 3.1.3. Forced Runs ( $\frac{1}{2}f_0, 1f_0, 2f_0, 4f_0, 8f_0, 16f_0$ )

Having determined the level for  $f_0$  that matches the kinetic energy between the MRI-only and hydro-only runs, we initiate six MHD runs with the amplitude of the forcing set at  $\frac{1}{2}f_0, 1f_0, 2f_0, 4f_0, 8f_0$ , and  $16f_0$ . We are particularly interested in the behavior of the magnetic fields and the angular momentum transport obtained in these simulations.

Figure 4 shows the time evolution of the volume average of  $B_z^2$  for the fiducial unforced MRI simulation,

<sup>3</sup> Alternatively, we could define equivalence via the rate of energy input. This, however, is harder to measure in the MRI case.

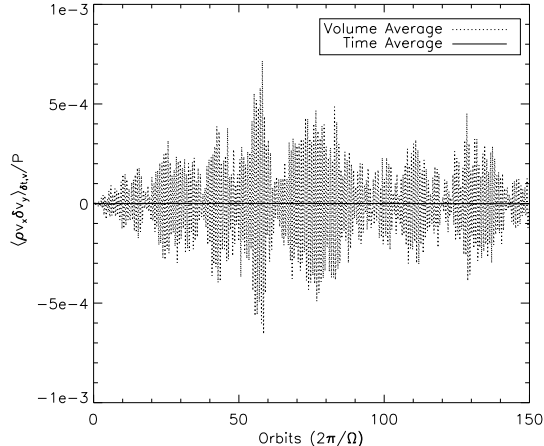


FIG. 3.— Time and volume averages (equations 9 and 8) of the transport coefficient,  $\alpha$  (equation 1) for the purely hydrodynamical, large scale forcing simulation (HL). No transport is induced by the hydrodynamic forcing when it is employed on its own.

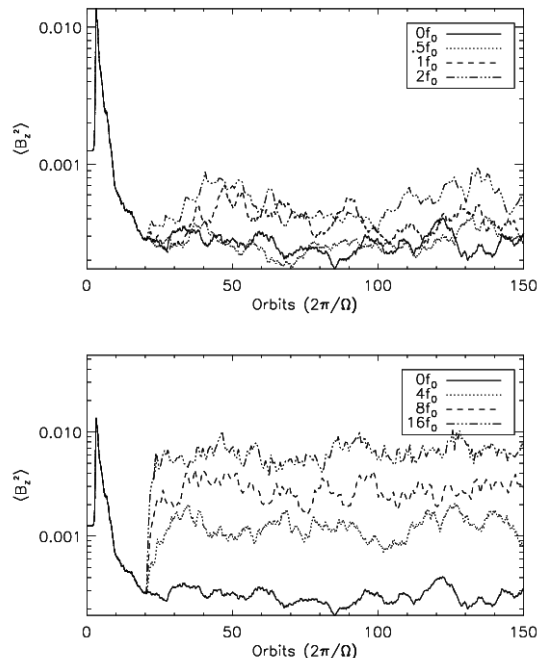


FIG. 4.— Evolution of  $B_z^2$ , averaged over the simulation volume, for all MHD simulations including large scale forcing ( $0f_0, 1f_0, 2f_0, 4f_0, 8f_0, \& 16f_0$ ). All forcing strengths above the  $1f_0$  case induce noticeable increases in field strength.

together with the results from the six simulations with variable forcing levels. The amplitude of the vertical magnetic field component is statistically similar (given the large fluctuations) for the  $\frac{1}{2}f_0$  and  $1f_0$  cases as compared to the unforced MRI-only run. For stronger forcing ( $2f_0$  and above)  $B_z^2$  clearly exceeds that which would be generated by the action of the MRI alone. Very roughly the energy in the vertical field scales linearly with the amplitude of forcing (recall that the forcing amplitude is defined via the energy in fluid motions).

Our interpretation of the behavior of  $B_z^2$  in the presence of forcing is that the existence of external hydrodynamic turbulence introduces more turnover in the verti-

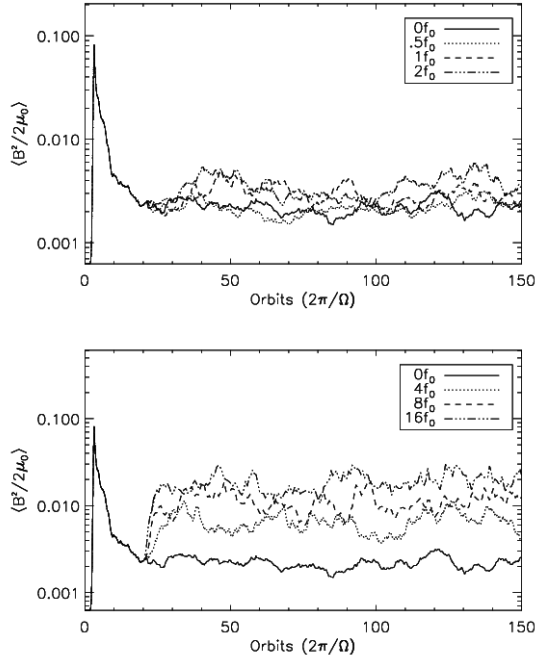


FIG. 5.— Evolution of  $B^2/2\mu_0$ , the total energy in the magnetic field within the simulation volume. Results are shown for the unforced and all forced MHD runs in the large scale forcing simulations ( $0f_0, 1f_0, 2f_0, 4f_0, 8f_0, \& 16f_0$ ). For forcing amplitudes greater than  $4f_0$  we see a sharp rise in the strength of the magnetic field consistent with the idea that a new MRI exponential growth phase is initiated, subsequent to which the new saturation level is maintained.

cal direction via random fluid motions. This increase in the “kneading” of the  $z$  component of the magnetic field by the forced turbulence increases  $B_z^2$ . Since the generation of vertical field by the MRI is relatively weak (this is reflected in the fact that, at saturation, only a small fraction of the magnetic energy in MRI simulations is in the  $z$  component) it is no surprise that modest levels of isotropic hydrodynamic turbulence suffice to generate higher  $B_z^2$ .

Figure 5 displays the total magnetic field energy density for all the MHD simulations. For all runs we see an increase in the total field energy as  $f_0$  increases. For the weaker forcing simulations (those up to  $2f_0$ ) the timescale over which the disk adjusts to a new quasi-steady state (with a higher saturation level) is relatively long – typically tens of orbital periods. Somewhat different behavior is seen in the very strongly forced runs ( $4f_0$  and above). In these cases the field adjusts almost immediately to a higher value once the forcing is turned on, and these stronger fields are then sustained on average for the duration of the simulation. What may be happening here is that the enhanced  $B_z$  created by the forced turbulence has “resparked” the rapid growth phase of the MRI allowing for more rapid adjustment of the field configuration.

The presence of stronger magnetic fields in the stirred runs raises the question of whether the resulting turbulence (i) retains the character of the MRI, (ii) is more similar to non-magnetic turbulence, or (iii) is distinct from either. We have attempted to quantify the character of the turbulence in two ways. First, we study the global characteristics of the turbulence, concentrating on

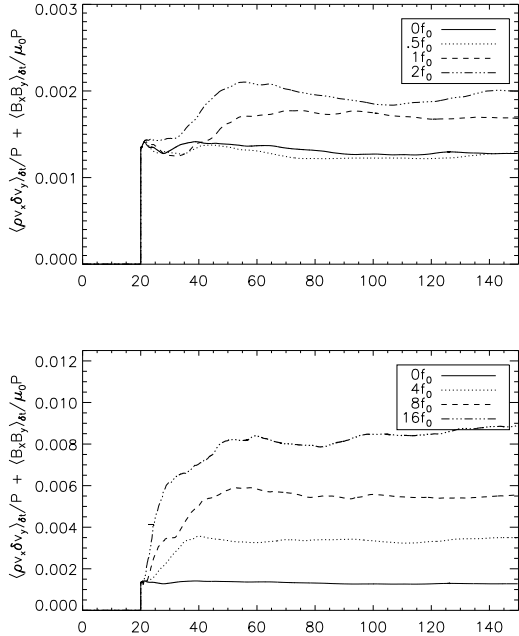


FIG. 6.— Running time average of  $\alpha$  for all large scale forcing, MHD simulations ( $0f_0$ ,  $1f_0$ ,  $2f_0$ ,  $4f_0$ ,  $8f_0$ , &  $16f_0$ ).

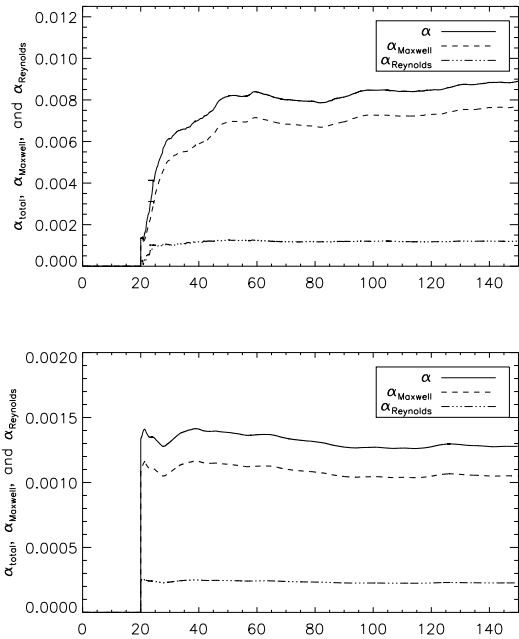


FIG. 7.— Running time average of the Maxwell and Reynolds components of  $\alpha$  as well as the total  $\alpha$  for the unforced MRI simulation and the run with the strongest large scale forcing ( $16f_0$ ). The magnetic component of the transport remains dominant in both the unforced MRI run and in the most strongly forced case.

the strength of angular momentum transport and how that stress is partitioned between Maxwell and Reynolds components. A notable feature of the MRI is that the stress is dominated by the Maxwell contribution, although the Reynolds stress is also non-zero. Second, we look at the structure of the turbulent flow as measured by the power-spectrum of various quantities.

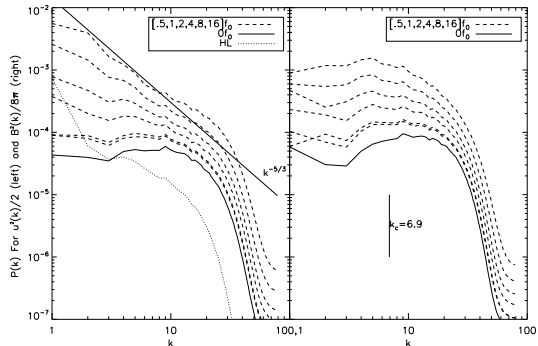


FIG. 8.— Power spectra of the kinetic energy (left panel) and the magnetic field energy density (right panel) in the large scale forcing simulations. The spectra have been averaged over orbits 130-140. HL is the hydrodynamic only large scale forcing simulation,  $0f_0$  is the unforced MRI simulation and the remaining curves show the forced, large scale simulations. The expected Kolmogorov slope has been plotted for the kinetic energy spectra and the location of the critical wavelength has been plotted in the panel corresponding to the magnetic field spectra. In all cases the total energy in the system increases with forcing amplitude. There is a transition between MRI-like and hydrodynamic behavior visible in the kinetic energy spectra at large spatial scales.

Figure 6 shows the time evolution of the equivalent  $\alpha$  parameter for all of the runs that incorporate large-scale forcing. The division between magnetic and hydrodynamic stress is shown in Figure 7 for the unforced ( $0f_0$ ) and most strongly forced ( $16f_0$ ) cases. Forcing boosts the strength of angular momentum transport once it is as strong ( $1f_0$ ) or stronger than the MRI in terms of the saturated equivalent kinetic energy. The derived  $\alpha$  increases steadily with the forcing level up to the  $16f_0$  run, which displays a value of  $\alpha$  about 6 times larger than the unforced MRI-only simulation. The fraction of the transport contributed by Maxwell stress as compared to Reynolds stress remains surprisingly constant between the unforced and maximally forced cases. Even though we are imposing external forcing – in some cases at quite a vigorous level – the transport is still determined by the magnetic field, and appears to retain the characteristic behavior expected from the MRI.

We can also quantify the structure of the turbulence via power spectra of the velocity and magnetic fields. Figure 8 shows power spectra for both the kinetic energy and (where appropriate) magnetic energy density for the hydrodynamic reference simulation, for the unforced MRI run, and for all of the large-scale forcing simulations. For the hydrodynamic simulation (shown in the left panel Figure 8), we see that the kinetic energy is dominated by the wavelength which corresponds roughly to the box size at which power is injected. For wavenumbers between  $k = 3$  and  $k = 30$  the spectrum is approximately of the Kolmogorov form ( $\propto k^{-5/3}$ ). For the MRI-only run the spectra of the kinetic energy and magnetic fields are quite similar – they are essentially flat at large scales ( $k < 20$ ) with a subsequent sharp decline toward the dissipation scale. When forcing is included in the MRI simulation we see the same pattern of behavior discussed above in the context of  $\alpha$ . For the relatively weakly forced runs ( $0.5f_0$  and  $1f_0$ ) both the kinetic and magnetic power spectra are only slightly modified from the MRI-only case. For stronger forcing we find that the large-scale *hydrodynamic* structure of

the turbulence (quantified by the kinetic energy power spectrum) increasingly resembles that of non-magnetized turbulence. For the  $16f_0$  run the large-scale slope is reasonably close to the Kolmogorov expectation. The power spectrum of the magnetic fields, on the other hand, looks like a scaled version of the MRI-only run even up to the strongest forcing levels. There is some evidence for a shift of the peak power toward lower  $k$ , which would be consistent with the MRI operating at larger scales in the presence of stronger magnetic fields. We interpret these results as suggesting that the *magnetic* character of the turbulence remains similar (at all scales) to that generated by the MRI even in the presence of strong hydrodynamic forcing. The stronger magnetic fields generated by adding forcing then merely scale up the angular momentum transport efficiency from the value expected in the absence of such effects.

Figure 9 shows a slice of the density profile in the  $x$ - $y$  ( $r$ - $\phi$ ) plane at 150 orbits for simulations HL,  $0f_0$ ,  $4f_0$ , and  $16f_0$ . The dominant effect of the shear is clearly visible – the turbulence is stretched out into ribbons elongated in the azimuthal direction. Comparing the plots, about the only feature that is visually apparent is the increase in the large-scale power (here in the density field) as the strength of hydrodynamic forcing is increased. The most strongly forced run displays substantially greater density contrasts, and it is clear that the large-scale morphology of the flow has been altered significantly from the MRI-only case. Nevertheless, as discussed above, on the (somewhat smaller) scales that are most important for angular momentum transport the MHD properties of the flow are apparently not significantly modified.

To quantify the relationship between the strength of imposed forcing and the resulting physical quantities ( $\alpha$ , kinetic energy density etc) we measure the ratio of the mean quantities in the forced to the unforced run. This ratio, defined as,

$$T(f_0) = \frac{\langle F(t_{\text{final}}, f_0) \rangle_{\delta t}}{\langle F(t_{\text{final}}, f_0 = 0) \rangle_{\delta t}} \quad (10)$$

is plotted in Figure 10 for  $\alpha$ , its decomposition into Maxwell and Reynolds stresses, the total magnetic field energy, and the total kinetic energy. It is evident that, to a good approximation, the additional energy injected via the forcing simply raises the saturated value of the kinetic energy in the same manner as one would expect for purely hydrodynamic runs – i.e. the  $16f_0$  run, which would have 16 times the kinetic energy of the MRI-only run in the hydrodynamic limit, does indeed yield that enhancement in the presence of MHD. The fact that these are MHD runs, in which the dissipation properties of turbulence could in principle differ significantly from the hydro only case, does not appear to make a substantial difference. This is similar to the situation studied in the context of molecular clouds — where MHD and hydrodynamic turbulence have comparable decay rates (Mac Low et al. 1998; Stone, Ostriker & Gammie 1998) — though here the fluid motions are highly subsonic.

As noted previously, all of the magnetic quantities, together with the Reynolds stress (which is an approximately fixed fraction of the total stress) increase in unison as the forcing strength increases. The relationship is roughly linear in the value of the forcing parameter  $f_0$ , though with a smaller slope than the 1:1 relation-

ship seen for the kinetic energy. A forcing strength that yields an order of magnitude increase in the saturated kinetic energy density results in about a factor 4 increase in the the magnetic field energy density and in all of the components of  $\alpha$ .

### 3.1.4. Large Scale Runs With Different Prandtl numbers

A number of recent studies provide evidence that the magnetic Prandtl number,

$$\text{Pm} \equiv \frac{\nu}{\eta} \quad (11)$$

is an important parameter whose value affects the saturation level of MHD turbulence initiated by the MRI (Lesur & Longaretti 2007; Fromang et al. 2007)<sup>4</sup>. This dependence is of interest since the predicted value of Pm varies substantially between the inner regions of black hole accretion disks (where  $\text{Pm} \gg 1$ ) and the outer region (Balbus & Henri 2008). In all of the simulations performed above our *hyperviscous* Prandtl number  $\nu_h/\eta_h$  was equal to one. To explore the affects of varying the the Prandtl number we ran two simulations, one in which we increased the value of our viscosity coefficient by a factor of four and one in which we reduced our resistive coefficient by a factor of four. This change in coefficients allowed for an effective span of 16 in Prandtl number. We ran both of these simulations with a forcing amplitude of  $2f_0$  as this marked the lowest forcing level for which significant differences with the unforced runs were observed. We ran these simulations from our fiducial start point at 20 orbits out to 150 orbits and labeled them  $2f_0p4$  and  $2f_0p.25$ .

Figure 11 shows the volume averaged magnetic energy density for simulations  $2f_0$ ,  $2f_0p4$ , and  $2f_0p.25$ . In this comparison our ‘fiducial’ model is the  $2f_0$  run with a Prandtl number of one. We observe sustained turbulence out to 150 orbits in all cases, implying that our effective Reynolds number (which should be boosted somewhat by our use of hyperviscosity rather than a regular viscosity) is high enough that sustained turbulence is possible even for  $\text{Pm}_h = 0.25$ , i.e. that we are in the large Reynolds number regime described by Fromang et al. (2007). In fact, no clearly significant differences are seen between the  $\text{Pm}_h = 0.25$  and  $\text{Pm}_h = 1$  runs. For  $\text{Pm}_h = 4$ , on the other hand, we see an increase of about a factor of 2-2.5 in the magnetic field energy and angular momentum transport efficiency. Although the use of hyperviscosity and hyperresistivity means that our runs are not equivalent (and indeed are less physical) to those of Lesur & Longaretti (2007) and Fromang et al. (2007) this trend is consistent with those previous studies which show an increase in saturation level with increased Prandtl number. We borrow the same interpretation: values of  $\text{Pm} > 1$  result in strong viscous damping at scales larger than the magnetic field dissipation scale. This suppresses magnetic field dissipation at small scales, and favors an inverse cascade of magnetic energy to larger scales and an attendant increase in  $\alpha$ .

While we see an increase in the saturation level for the higher Prandtl number simulation the the underlying behavior remains the same as that seen in the large

<sup>4</sup> The value of Pm also affects the properties of non-rotating, driven MHD turbulence (Schekochihin et al. 2004; Isakov et al. 2007).



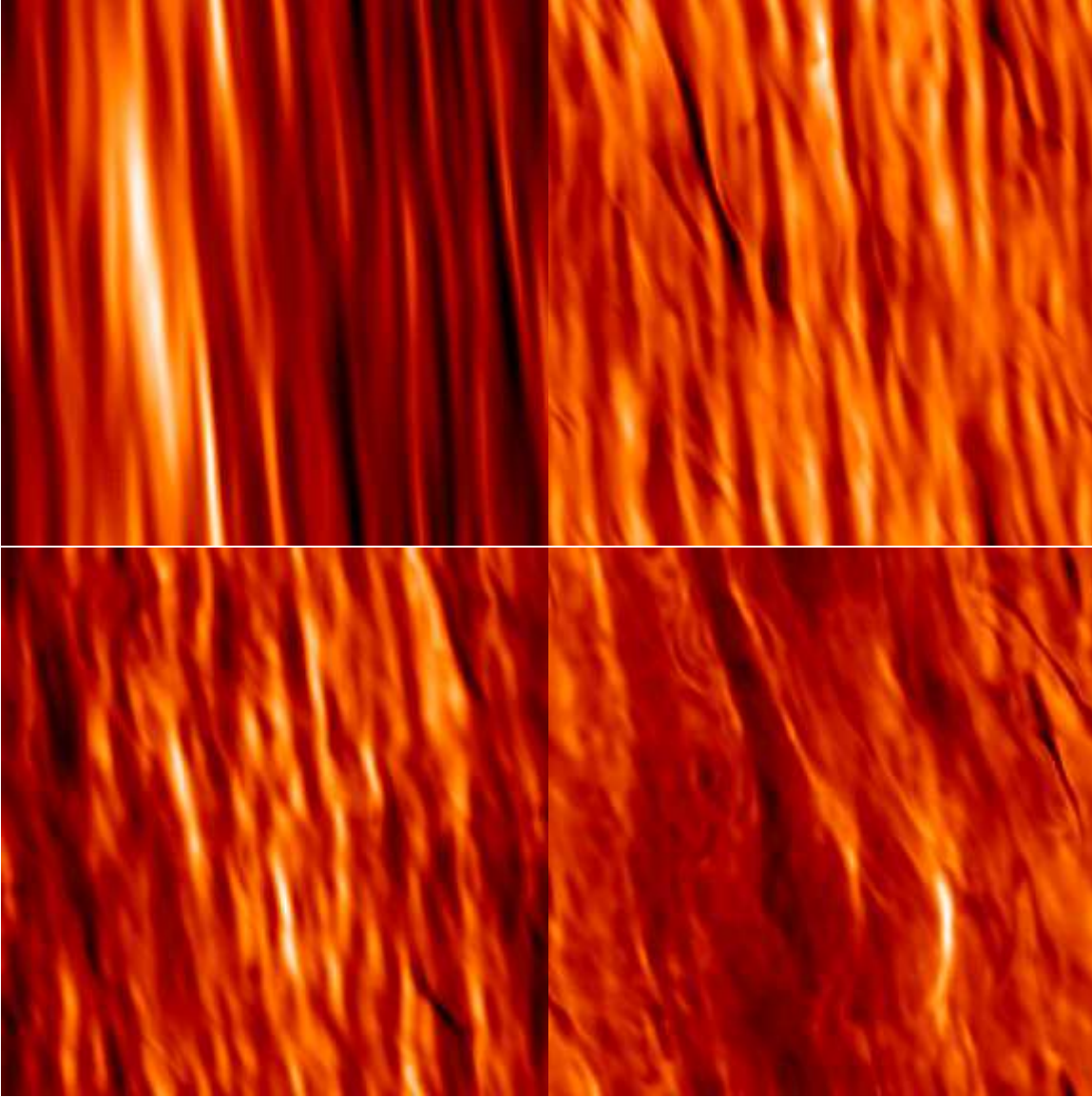


FIG. 9.— Density slices at 150 orbits in the  $xy$  plane taken from simulations HL (upper left),  $0f_0$ ,  $4f_0$ , &  $16f_0$ .

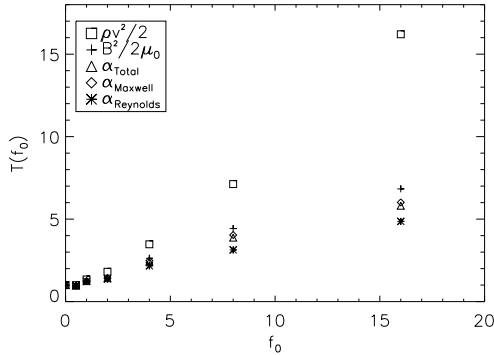


FIG. 10.— The average values of the magnetic field energy density, kinetic energy and components of  $\alpha$  from the large scale forcing runs, normalized to the results of the unforced MRI simulation. The forcing strength is represented on the  $x$ -axis by the value of the normalization parameter for the forcing  $f_0$ .

scale forcing runs. For both runs with altered Prandtl numbers the transport is still dominated by the Maxwell

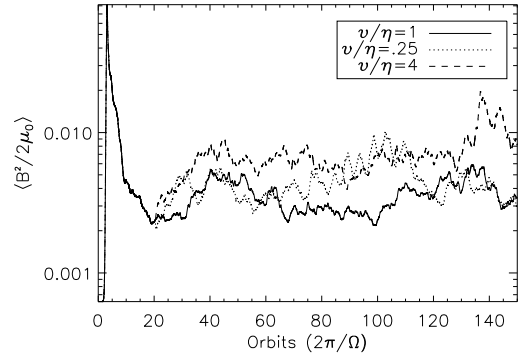


FIG. 11.— Evolution of the magnetic field energy density ( $B^2/2\mu_0$ ) for the simulations with altered Prandtl numbers ( $\nu/\eta$ ). All three runs used  $2f_0$  as the forcing amplitude.

stresses and the proportion of Maxwell to Reynolds stress remains the same. We find no significant differences in the behavior of the field components or the power spectra except that they are amplified in the the higher Prandtl

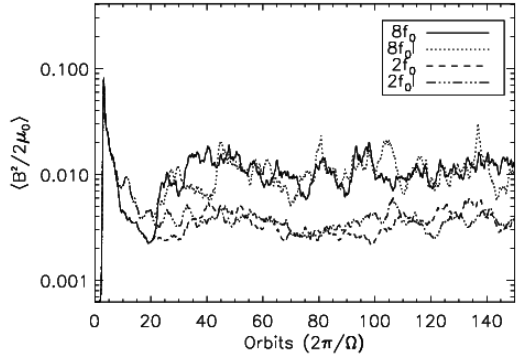


FIG. 12.— Evolution of the magnetic field energy density ( $B^2/2\mu_0$ ) for the simulations with orbital period forcing variations. The results are compared to those from the equivalent large scale simulations in which the forcing was varied on the timescale of the simulation timestep. The results marked with an 'l' denote the orbital period simulations. No significant differences are seen.

number run.

### 3.1.5. Large Scale Runs With Orbital Period Forcing

In the large-scale forcing runs described above the vectors which describe the instantaneous turbulent driving are chosen anew at each timestep. The forcing is then temporally uncorrelated with any characteristic frequency of the disk. To check whether the results depend upon this feature we repeated some of the runs with the correlation time for the forcing set to be the orbital period<sup>5</sup>. We ran simulations at two times and eight times the reference forcing amplitude with orbital period forcing ( $2f_0l$  and  $8f_0l$ ) and compared them to the standard runs with time step forcing variations. Figure 12 shows the volume averaged magnetic energy density in the simulations with orbital period forcing variation compared to their standard counterparts. We find no discernible differences in the magnetic field, transport coefficients, or spectra in the case of orbital period variations. Both the behavior and the saturation amplitudes agree. Once again the Maxwell stresses dominate the transport.

## 3.2. Small Scale Forcing Runs

We have also considered the effects of forcing on scales  $\lambda \ll H$ . Once again we begin by finding the strength of forcing that yields a saturated kinetic energy density that matches that obtained in a fiducial MRI-only simulation, except now we use a forcing function that injects power at wavenumbers around  $k = 40$ . The match we obtained was good at the  $\approx 20\%$  level. We found that the residual hydrodynamic  $\alpha$  in the purely hydro run was substantially higher than in the case with large scale forcing, but still negligible for our purposes (being two orders of magnitude below the MRI value).

Figure 13 and figure 14 show the time evolution of  $B_z^2$  and  $B^2/2\mu_0$  for the small scale forcing simulations. We considered a more limited range of forcing strengths between  $1sf_0$  and  $4sf_0$ . Within this range, there are some differences between the behavior of the disk subject to large and small scale forcing. Most notably, although

<sup>5</sup> We adopted this timescale since it is a well-defined characteristic frequency for an accretion disk. Since it is also the resonant frequency, any effects due to changing the timescale are likely to be maximized by adopting orbital period scale forcing.

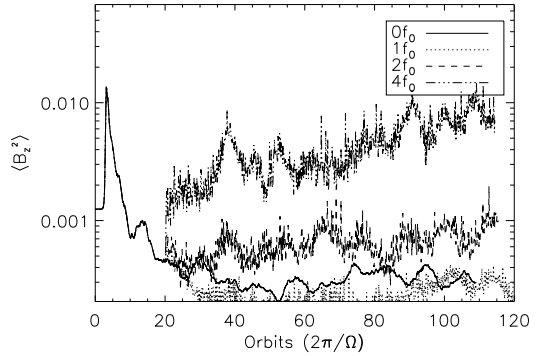


FIG. 13.— Evolution of  $B_z^2$  for the simulations with small scale forcing ( $0sf_0$ ,  $1sf_0$ ,  $2sf_0$ , &  $4sf_0$ ).

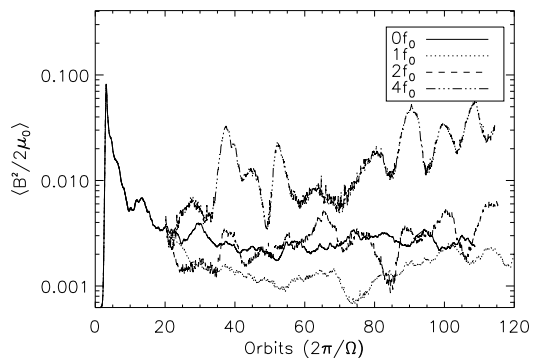


FIG. 14.— Evolution of the magnetic field energy density  $B^2/2\mu_0$  for the simulations with small scale forcing ( $0sf_0$ ,  $1sf_0$ ,  $2sf_0$ , &  $4sf_0$ ).

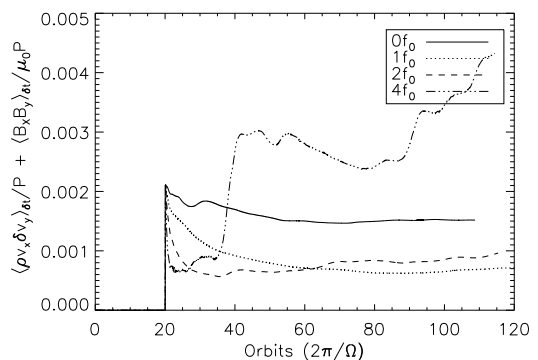


FIG. 15.— Running time average of  $\alpha$  for the simulations with small scale forcing ( $0sf_0$ ,  $1sf_0$ ,  $2sf_0$ , &  $4sf_0$ ). The lowest two forcing strengths result in a suppression of angular momentum transport.

relatively weak levels of forcing (the  $2sf_0$  run) do increase the value of the vertical magnetic field, this is not accompanied by any significant increase in the total magnetic field. The strongest level ( $4sf_0$ ) of forcing *does* amplify all components of the magnetic field. We also observe larger fluctuations in magnetic field strength as compared to the equivalent large-scale forcing simulations.

The stress within the simulated patch of disk largely follows the total magnetic field strength. Figure 15 shows the running time average of the equivalent  $\alpha$  parameter

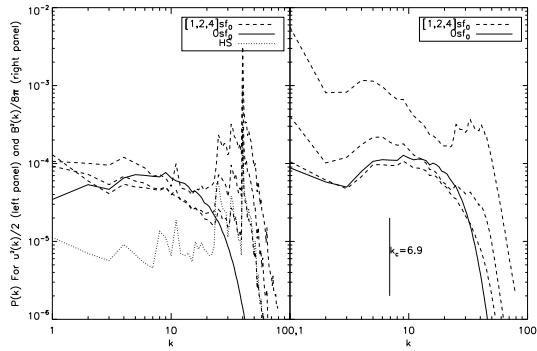


FIG. 16.— Power spectra of the kinetic energy (left panel) and the magnetic field energy density (right panel) for simulations with small scale forcing. In these runs the forcing is applied at a wavenumber  $k = 40$ . The spectra have been averaged over orbits 95-105. HS is the hydrodynamic only simulation with small scale forcing,  $0s f_0$  is the unforced MRI run, while the remaining curves correspond to the small scale, forced MRI runs. Unlike in the large scale forcing runs Kolmogorov spectra are not observed at large scales, and there is a marked accumulation of power close to the injection wavenumber. Power in the large scale magnetic field is essentially unaltered by the forcing except in the highest amplitude forcing run.

for the different simulations. The average  $\alpha$  is lower in the weakly forced runs ( $1s f_0$  and  $2s f_0$ ) than in the unforced simulation, and only shows significant enhancement in the  $4s f_0$  case. In this case it is clear that the value of  $\alpha$  has not converged by the end of the simulation. We note that in all cases – including those where the forcing appeared to suppress the MRI – the transport remains dominated by Maxwell stresses.

Figure 16 shows the power spectra of the kinetic energy (left panel) and magnetic energy density (right panel) for all of the small scale forcing simulations. The accumulation of power in the kinetic energy spectrum at scales close to the forcing scale of  $k = 40$  is very obvious in all the forced runs, and on this scale the power in fluid motions greatly exceeds that which would be generated by the MRI. In the hydro-only run power leaks out to larger scales, and results in a roughly flat power spectrum out to the box scale at  $k = 1$ . The spectra of the magnetic field energy are rather different. In the two most weakly forced runs the forcing increases the power close to the forcing scale, but diminishes or leaves roughly unaltered the power on larger scales. In particular, for these runs there is no increase in the power on the scales – comparable to the most unstable linear MRI modes – that are presumably most important for field evolution in a disk. Only for the strongest level of forcing ( $4s f_0$ ) do we see a clear increase in the power across all of the scales accessible to the simulation.

Based on these results, we conjecture that the impact of hydrodynamic forcing on the MRI varies depending on the effect that the forcing has on magnetic fields with scales comparable to the most unstable MRI wavelengths in the disk. Large scale forcing efficiently enhances the vertical magnetic field in the disk at quite moderate amplitudes, and essentially always boosts the strength of angular momentum transport. Power from small scale forcing primarily affects the structure of the turbulence at scales close to and below the injection scale, and, at least if the forcing is weak, relatively little power cascades back to large scales. There is no enhancement

of the field strength on the scales most important for growth of the MRI. Rather, the imposed turbulent motion on small scales acts to suppress the MRI, perhaps by enhancing magnetic field dissipation (the inverse of the Prandtl number effect discussed above), or perhaps by directly destroying the correlation between the radial and azimuthal field that is responsible for the Maxwell stress. Only if the small scale forcing is rather strong does enough power reach larger scales, at which point the MRI can be enhanced via the same mechanisms as apply in the large scale forcing runs.

#### 4. DISCUSSION

In this paper we have used local shearing-box simulations of accretion disks to study the interaction between the magnetorotational instability and hydrodynamic turbulence in disks where both coexist. We have studied both large scale forcing, in which energy is injected at scales  $\lambda \sim H$ , the disk scale height, and to a more limited extent small scale forcing where  $\lambda \ll H$ . We find that the effect of the additional energy input from the hydrodynamic turbulence on the MRI varies depending upon both the strength of the forcing and, to some extent, on its spatial structure.

For large scale forcing the results are straightforward. When hydrodynamic forcing is “weak” – in the sense that the hydrodynamic forcing, on its own, yields a saturated kinetic energy density in the disk that is less than or equal to that generated by the MRI alone – the MRI is essentially unaffected at the level of precision accessible to our simulations. This result is no surprise. The MRI is a robust instability, which is present within differentially rotating flows containing almost arbitrary magnetic field geometries (Balbus & Hawley 1998). Low amplitude random perturbations do not affect it. When stronger forcing is imposed, we find that both the saturation value of the magnetic field and the strength of angular momentum transport can be substantially boosted. The flow retains many of the characteristics of the MRI – such as a similar ratio between magnetic field strength and  $\alpha$ , and a similar ratio of Maxwell to Reynolds stresses, even in a regime when the hydrodynamic forcing (which, by itself, yields no transport at all) is formally dominant. The application of heuristic dynamo arguments to the MRI is suspect (Balbus & Hawley 1998), but we tentatively attribute the numerical behavior to the more efficient regeneration of vertical field in the presence of hydrodynamic turbulence.

The small scale forcing results are more nuanced, and given the limited number of simulations we have performed should be regarded as preliminary. In this regime we find that only the strongest level of forcing boosts the strength of angular momentum transport, whereas lower forcing levels actually suppress transport. We attribute this different behavior to the fact that there are two important considerations that affect the saturation amplitude of the MRI. One is the strength of the vertical magnetic field on relatively large scales (typically a fraction of  $H$ ), similar to the most unstable linear MRI wavelengths. Enhancement of the vertical field on this scale – which is readily accomplished with large scale forcing but which requires an inverse cascade in the small scale case – boosts the strength of the MRI. The second is the dissipation scale. Turbulent driving that increases

the amplitude of kinetic energy at or near this scale may enhance magnetic field dissipation, ultimately reducing the saturation level of magnetic fields in the disk as a whole. This is the inverse of the physical process invoked to explain the dependence of  $\alpha$  on the magnetic Prandtl number (Lesur & Longaretti 2007; Fromang et al. 2007). Small scale forcing may also directly destroy the correlations between  $B_r$  and  $B_\phi$  that result in Maxwell stress.

Our results allow us to infer which additional physical effects are likely to be able to affect the MRI in accretion disks. We first observe that if the additional turbulence is “powered” by the MRI itself (i.e. if the turbulence derives energy from the gravitational potential well as a result of MRI-driven angular momentum transport), then generically it is unlikely to be as powerful as the MRI. Such turbulence will have at most a small effect on the magnitude and character of angular momentum transport. As an explicit example, we would not expect an MRI-active disk that was additionally unstable to convection to differ much from one in which the vertical structure was stable against convective motions.

We can also consider sources of turbulence that are independent of the MRI, in the sense that they would exist even in a (hypothetical) disk that was absent magnetic fields entirely. Physical examples include self-gravity, thermal instability, and turbulence stirred up by the interaction between the gaseous and solid components of protoplanetary disks. There is no reason why these sources of turbulence should not generate fluid motions of greater amplitude than those produced by the MRI

(this is likely to be the case in self-gravitating disks near the fragmentation threshold, and locally in some regions of protoplanetary disks). In this regime, our results suggest that the MRI will have a non-trivial interaction with the hydrodynamic turbulence. If the forcing occurs at scales comparable to  $H$  or larger, we find that the interaction will likely boost the strength of angular momentum transport. Even for quite violent forcing – up to an order of magnitude in excess of that required to produce parity with the MRI – we find that it is most accurate to think of the coupled system as one with boosted MHD turbulence, rather than as a hydrodynamic system passively advecting magnetic fields. Conversely, small scale forcing, unless it is very strong, may actually suppress the saturation level of magnetic fields in the disk and their associated angular momentum transport.

This work was supported by NASA under grants NNG04GL01G and NNX07AH08G from the Astrophysics Theory Program, and by the NSF under grant AST 0407040. Simulations were run on the NSF’s TeraGrid platforms, and on NASA’s Columbia system. We thank Brian Morsony for useful discussions, and the referee for many helpful suggestions including the idea of looking at small scale driving. We are grateful to Peter Ruprecht, James McKown, and the support teams at NCSA and Columbia for invaluable assistance with the computations, and the authors and users of PENCIL for help with the code.

#### REFERENCES

- Armitage, P. J. 1998, *ApJ*, 501, L189  
 Balbus, S. A., & Hawley, J. F. 1991, *ApJ*, 376, 214  
 Balbus, S. A., & Hawley, J. F. 1998, *Reviews of Modern Physics*, 70, 1  
 Balbus, S. A., & Henri, P. 2008, *ApJ*, 674, 408  
 Bate, M. R., Ogilvie, G. I., Lubow, S. H., & Pringle, J. E. 2002, *MNRAS*, 332, 575  
 Brandenburg, A., Nordlund, A., Stein, R. F., & Torkelsson, U. 1995, *ApJ*, 446, 741  
 Brandenburg, A. 2001, *ApJ*, 550, 824  
 Brandenburg, A. & Sarson, G. 2002, *Phys. Rev. Lett.*, 88, 5  
 Chandrasekhar, S. 1961, *Hydrodynamic and hydromagnetic stability*, International Series of Monographs on Physics, Oxford: Clarendon  
 Cuzzi, J. N., Dobrovolskis, A. R., & Champney, J. M. 1993, *Icarus*, 106, 102  
 Fromang, S., Balbus, S. A., Terquem, C., & De Villiers, J.-P. 2004, *ApJ*, 616, 364  
 Fromang, S., Papaloizou, J. 2007, *A&A*, 476, 1113  
 Fromang, S., Papaloizou, J., Lesur, G., & Heinemann, T. 2007, *A&A*, 476, 1123  
 Gammie, C. F. 2001, *ApJ*, 553, 174  
 Gardiner, T. A., & Stone, J. M. 2005, in “Magnetic Fields in the Universe: From Laboratory and Stars to Primordial Structures”. AIP Conference Proceedings, Volume 784, p. 475  
 Haugen, N. E. L., Brandenburg, A., & Dobler, W. 2004, *Phys. Rev. E.*, 70, 016308  
 Hawley, J. F. 2000, *ApJ*, 528, 462  
 Hawley, J. F., Gammie, C. F., & Balbus, S. A. 1995, *ApJ*, 440, 742  
 Hirose, S., Krolik, J. H., & Stone, J. M. 2006, *ApJ*, 640, 901  
 Iskakov, A. B., Schekochihin, A. A., Cowley, S. C., McWilliams, J. C., & Proctor, M. R. E. 2007, *Physical Review Letters*, 98, 208501  
 King, A. R., Pringle, J. E., & Livio, M. 2007, *MNRAS*, 376, 1740  
 Johansen, A. & Klahr, H. 2005, *ApJ*, 634, 1353  
 Lesur, G., & Longaretti, P.-Y. 2007, *MNRAS*, 378, 1471  
 Mac Low, M.-M., Klessen, R. S., Burkert, A., & Smith, M. D. 1998, *Phys. Rev. Lett.*, 80, 2754  
 Papaloizou, J. C. B., & Nelson, R. P. 2003, *MNRAS*, 339, 983  
 Pessah, M. E., Chan, C., & Psaltis, D. 2008, *MNRAS*, 383, 683  
 Piontek, R. A., & Ostriker, E. C. 2005, *ApJ*, 629, 849  
 Rice, W. K. M., Lodato, G., & Armitage, P. J. 2005, *MNRAS*, 364, L56  
 Sano, T., Inutsuka, S., Turner, N. J., & Stone, J. M. 2004, *ApJ*, 605, 321  
 Schekochihin, A. A., Cowley, S. C., Taylor, S. F., Maron, J. L., & McWilliams, J. C. 2004, *ApJ*, 612, 276  
 Shakura, N. I., & Sunyaev, R. A. 1973, *A&A*, 24, 337  
 Spruit, H. C., Matsuda, T., Inoue, M., & Sawada, K. 1987, *MNRAS*, 229, 517  
 Sridhar, S., & Goldreich, P. 1994, *ApJ*, 432, 612  
 Stone, J. M., & Balbus, S. A. 1996, *ApJ*, 464, 364  
 Stone, J. M., Ostriker, E. C., & Gammie, C. F. 1998, *ApJ*, 508, L99  
 Toomre, A. 1964, *ApJ*, 139, 1217  
 Winters, W. F., Balbus, S. A., & Hawley, J. F. 2003, *MNRAS*, 340, 519  
 Velikov, S. 1959, *Jnl. Expl. Phys. (USSR)*, 36, 1398  
 Wisdom, J. & Tremaine, S. 1988, *AJ*, 95, 925